SOFT ROBOTICS
Volume 8, Number 1, 2021

DOI: 10.1089/soro.2019.0080

SoRo
Soft Robotics

*ORIGINAL ARTICLE*

# Tendon-Driven Jamming Mechanism for Configurable Variable Stiffness

Jaehyeok Choi,[1,2,*] Dae-Young Lee,[1–4,*] Jun-Hyeok Eo,[5] Yong-Jai Park,[1,5] and Kyu-Jin Cho[1,2,6]



## Abstract

Stiffness transition of a soft continuum body is an essential feature for dexterous interaction with an unstructured environment. Softness ensures safe interaction, whereas rigidness generates high force for movement or manipulation. Vacuum-based granular jamming is a widely used technique for on-line stiffness transition because of its high reconfigurability and intuitive driving method. However, vacuum driving method produces limited force levels, and the heavy weight and bulky size are unfavorable for portable applications. In this work, we propose a tendon-driven jamming mechanism for configurable variable stiffness. Compared with a vacuum system, an electric motor-tendon drive system has the benefits of force, bandwidth, size, and weight, but has different force characteristics for distribution, directionality, and transmissibility. In this study, a long snake-like shape is chosen instead of a lump shape for compatibility with tendon-drive characteristics. The snake-like shape is likely to cause buckling under the tendon force as the length increases, making the system extremely unstable. Implanting skeletal disk nodes in the structure is our solution to the buckling phenomenon by maintaining the tendon path in the desired position and for distributing the force evenly, thereby achieving stable stiffness transition capabilities for long free-curved shapes. As a proof of concept, a soft wearable device for wrist support is presented using the proposed variable stiffness mechanism. The weight of the device is 184 g, including the actuators, and it can support 2 kgf. Furthermore, the stiffness transition is completed within 2 s, thus achieving quick responses.

**Keywords:** granular jamming, tendon-driven, continuum structure

## Introduction

Muscular systems change their own stiffness to effectively interact with unstructured environments; these systems use softness to safely adapt to the environment and rigidness to achieve fast and precise movements or manipulations. Soft robotics, an emerging concept in robotics design, inherits the adaptability of a natural body by accepting highly flexible and stretchable materials as body elements. With the benefit of softness, soft robots have the advantage of being suitable for atypical environments, so they have been developed in various forms.[1–3] However, the lack of appropriate rigidity seriously limits the performance of these systems. Soft structures tend to be deformed by external forces, making it difficult to transmit a force or maintain physical configuration.

To overcome this limitation, various variable stiffness techniques for soft and continuum bodies have been proposed.[4,5] Each variable stiffness technique has its own characteristics but can be categorized into two groups according to the driving principle: material-based variable stiffness using material phase transitions[6–13] and mechanically driven variable stiffness using mechanical interactions. Furthermore, the mechanically driven variable stiffness can be divided into two subgroups depending on the dependency of the stiffness and configuration: shape-confined variable stiffness

[1]Soft Robotics Research Center, Seoul National University, Seoul, Korea.
[2]Department of Mechanical and Aerospace Engineering, Seoul National University, Seoul, Korea.
[3]School of Engineering and Applied Sciences, Harvard University, Cambridge, Massachusetts, USA.
[4]Wyss Institute for Biologically Inspired Engineering, Harvard University, Cambridge, Massachusetts, USA.
[5]Department of Mechatronics, Kangwon National University, Gangwon-do, Korea.
[6]Institute of Advanced Machines and Design, Seoul National University, Seoul, Korea.
*These authors contributed equally to this work.

and configurable variable stiffness. Shape-confined variable stiffness cannot achieve shape change and stiffness independently because it typically uses a movement constraint induced by structural confinement.[14–17] Contrarily, configurable variable stiffness enables changes in the stiffness of arbitrary shapes without the accompanying motion.

Generally, shape-confined variable stiffness has either a fast or large stiffness transition capability. The confined configuration makes it easy to achieve mechanical advantages in force transmission by using the actuator force directly. Electromagnetic force-activated materials, such as magnetorheological/electrorheological fluids or electroactive polymer, an example of shape-confined variable stiffness, have been researched to achieve rapid stiffness tuning. This rapid stiffness tuning has been used to control the mechanical response,[18] or has combined with patterning strategy to improve the driving efficiency.[19] Artificial muscle actuators like McKibben pneumatic actuator or motor-tendon actuators were also used to build up a simple stiffness tuning system. The design parameters of the McKibben actuator were controlled to obtain the variable stiffness feature,[20] or several actuators were combined to achieve antagonistic pairs.[21,22] The motor-tendon-driven actuation was also employed for variable stiffness to provide fast and reliable transition.[23,24] These variable stiffness techniques have been mostly developed and utilized for special purposes. However, despite the technical advantages, they have been limited in application because the stiffness and configuration of the system are coupled.

Configurable variable stiffness can decouple stiffness and configuration using a body that can be mechanically locked in various configurations. Granular jamming, a representative case of configurable variable stiffness, achieves highly reconfigurable features by using freely movable granular particles as the media material. Furthermore, the distributed force applied to the body surface that packages the media material generates interlocking between the media materials and increases the stiffness of the entire system.[25–27] This intuitive drive mechanism and its simple structure allow the utilization of this technique to various research areas. Based on the stiffness tunable feature, granular jamming has been used for various purposes; by controlling the interaction with the external system, granular jamming has been used to grip objects of various shapes.[28–30] The selective stiffening method was used to adjust force transmission to achieve the desired motion.[31–33] Some studies have employed granular jamming for manipulator type structures[34–37] or for structural components to adjust the mechanical responses.[38–42]

However, granular jamming stiffness transition has an inherent problem in the flexibility of activation method selection. As mentioned, vacuum pressure is usually used to obtain an evenly distributed compressive force for the jamming effect. Since granular jamming uses the compressive force between the granular particles, when the pressure increases, the reaction forces between the particles, which increases the frictional force and consequently the stiffness, also increases. Therefore, it is necessary to increase the pressure to increase the stiffness. However, the vacuum drive presents difficulties in increasing the force because the maximum pressure is limited by the atmospheric pressure. To address this limitation, various concepts have been proposed such as exploiting geometrical advantages[43,44] or utilizing jamming of layers to increase the effect of friction.[45–50] While these methods have successfully resolved the stiffness limitation, they also limit the achievable configuration range or require an air pressure drive system, which is usually heavy and bulky, and it could be a burden to portable applications.[51]

In this work, we propose a tendon-driven jamming mechanism for configurable variable stiffness. Compared with a vacuum drive system, an electric motor-tendon drive system has beneficial features regarding force, bandwidth, size, and weight. However, the electric motor-tendon drive is normally not suitable for granular jamming because a tendon force is highly concentrated and has strong directionality, which cannot produce a uniformly distributed force on the body surface. Thus, the distribution of the tendon-driven force becomes a crucial issue for the proposed mechanism. In addition, the tendon force should be transmitted along the tendon path so that it is more concordant with a snake-like cylindrical body shape rather than the bulk shape commonly used for granular jamming. However, the attainable length of the system is seriously limited owing to the buckling phenomenon caused by the compressive tendon force.

In this study, we solve this problem by implanting skeletal disk nodes in a granular packaged snake-like soft continuum body. The skeletal disks are placed on a body at regular intervals with the granular particles, and the tendon penetrates the centers of these disks. As the tendon is pulled, the skeletal disks press the granular particles with a distributed force while maintaining the tendon path along the segmented lines connecting the centers of the disks. This allows the positions of neighboring skeletal disks to remain fixed with different angles. By accumulating these relative angles, the body can achieve a long free-curve shape in three-dimensional space and also have a stable stiffness transition feature.

The following sections address the details of this concept and the structural design of the proposed mechanism. The analytic estimation of the performance based on a simplified model of jamming transition and supporting experiments are also presented. As a case study, we present a soft wearable device for wrist support using the proposed variable stiffness mechanism. The weight of the device is 184 g, including the actuators, and it can support 2 kgf with 10 W of electrical power. Furthermore, the stiffness transition is completed within 2 s, thus achieving a quick response time.

## Design Principle and Geometrical Analysis

The key differences between the proposed tendon-driven jamming transition and conventional vacuum-driven methods are directionality and distribution of force. The vacuum applied to the granular particles induces a pressure in the boundary membrane, so that the force is always generated in the direction perpendicular to the membrane and is evenly distributed over the entire surface. Unlike a vacuum-driven force, the force applied by the tendon only acts on the tendon junction points in a direction parallel to the tendon.

The concentrated force may cause undesired deformations of the system, as depicted in Figure 1A, and the uncompressed regions of the particles can cause unintended low stiffness. Furthermore, since the tendon force is always applied in the shortening direction of the tendon, this force will cause buckling or break the structure as the tendon path cannot be regulated properly (Fig. 1B). Implantation of skeletal disk nodes in a soft continuum body is our solution to

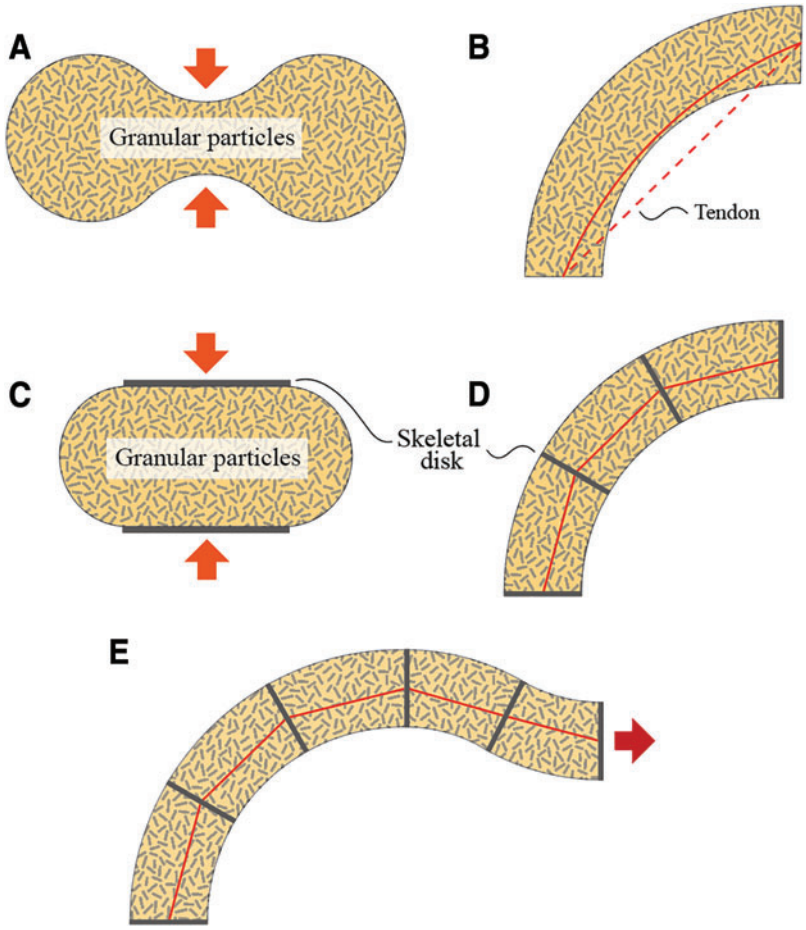


**FIG. 1.** Working principle of the tendon-driven jamming mechanism. **(A)** Deformation due to the concentrated force on granular particle pack. **(B)** Failure mode due to the wire route. **(C)** Structural solution for force distribution. **(D)** Proper tendon route directed by the disk. **(E)** Concept diagram of the whole structure. Color images are available online.



this problem. This improvement allows to distribute the tendon force and also prevents buckling by regulating the tendon path as shown in Figure 1C and D. Our observation indicates that the buckling phenomenon occurs when the direction of the tendon force is unduly different from the tangential direction of the body curve (normal direction to compress the granular material inside the body). We adjusted the tendon path by placing the rigid disks at regular intervals and made tendon junctions at the centers of the disks.

Figure 2A shows the basic unit of the proposed variable stiffness mechanism. Rigid plastic pellets were used as granular particles to minimize the effects of deformations of the media materials on stiffness performance. The skeletal disks were fabricated using a 3D printer (VerowhitePlus, Stratasys' Objet260), and the surface membrane was made of a common single-ply nonstretchable fabric. For the driving tendon, Nickel/Titanium kink-free wire was used to endure high tension. Figure 2B presents the design parameters that determine geometrical and mechanical characteristics: the granular filled height, $h_e$, the membrane height, $h_M$, and the disk diameter, $D$. The geometrical characteristic of the basic unit is analyzed under three main assumptions: (1) the granular material is incompressible, (2) the surface membrane is nonstretchable, and (3) the unit geometry is determined to have a minimum tendon length.

Figure 2C shows the schematic of the volume estimation. Through the simplification, the geometry of the unit can be described by the length of the tendon, $l$, the angle of the top disk, $\theta_D$, and the angle of the tendon $\theta_T$. The whole body of the unit can be assumed as an integration of segmented disks with the height of infinitesimal length along the tendon. As $\theta_D$ and $\theta_T$ change, this segmented disk is subjected to two types of deformation: shear translation and rotation. The diameters of the top and bottom side are assumed to be constant, and the translation is assumed to be the only factor that changes the volume determined by the angle between $\theta_T$ and the normal vector of the bottom side. Assuming a linear transition of the angle from the bottom to the top disk, the angle of the normal vector of the segment according to the base frame (bottom disk) can be given as:

$$\begin{aligned} \theta(s) &= \theta(0) + \frac{s}{l}\,\theta(l) \\ \theta(0) &= 0, \quad \theta(l) = \theta_D \end{aligned} \tag{1}$$

And the volume of the unit can be derived as:

$$\begin{aligned} \int_V d\tau &= \int_0^l \frac{\pi D^2}{2}\cos[\theta(s) - \theta_T]ds = \int_0^l \frac{\pi D^2}{2}\cos\left(\frac{s}{l}\theta_D - \theta_T\right)ds \\ &= \frac{\pi D^2}{2}\, l \left[\frac{\sin(\theta_D - \theta_T) + \sin\theta_T}{\theta_D}\right] \end{aligned} \tag{2}$$

And $l$ can be derived as:

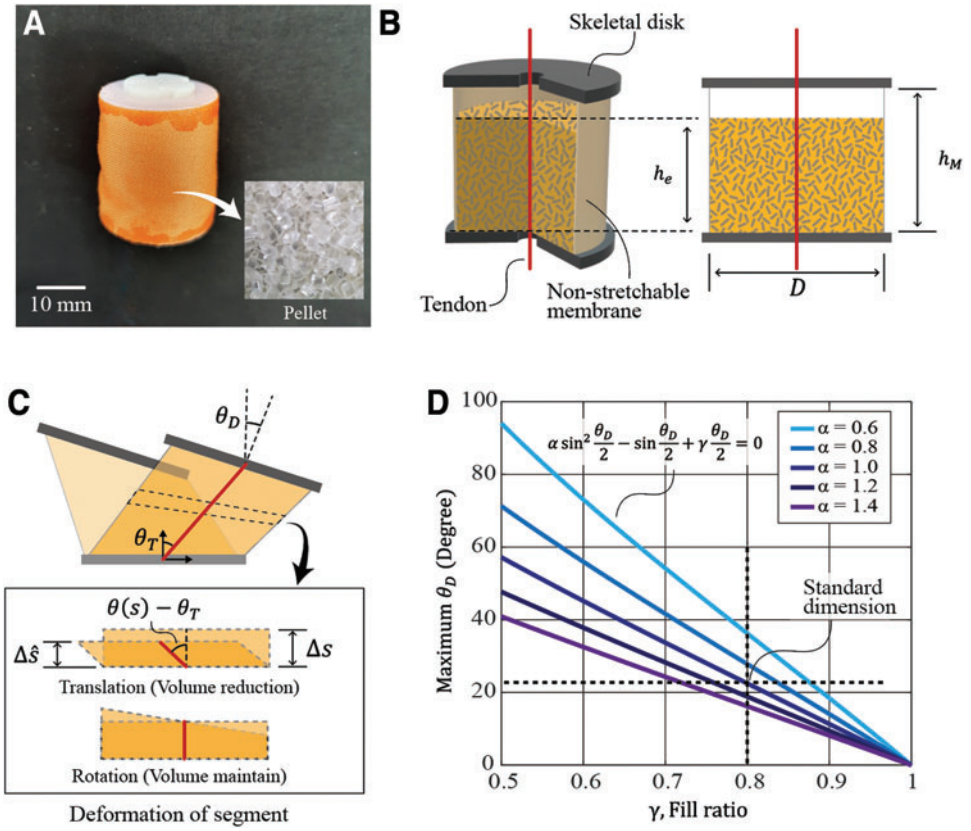


**FIG. 2.** Basic unit and core design parameter. **(A)** Photograph of the basic unit and pellets used as granular particles. **(B)** Schematic diagram of the unit and design parameters. **(C)** Graphical description of the parameters for the geometry analysis. **(D)** Trend of the maximum $\theta_D$ according to the aspect ratio, $\alpha$ and fill ratio, $\gamma$. Color images are available online.

$$\frac{\pi D^2}{2} h_e = \frac{\pi D^2}{2}\, l \left[\frac{\sin(\theta_D - \theta_T) + \sin\theta_T}{\theta_D}\right]$$
$$l = h_e \left[\frac{\theta_D}{\sin(\theta_D - \theta_T) + \sin\theta_T}\right] \tag{3}$$

From the assumption that $l$ has a minimum value, the relationship between $\theta_T$ and $\theta_D$ can be derived as:

$$\theta_T = \frac{\theta_D}{2} \tag{4}$$

Based on Equations (3) and (4), the maximum $\theta_D$ can be calculated from the geometrical constraint.

$$h_M \geq l + d\sin\frac{\theta_D}{2}$$
$$\alpha\sin^2\frac{\theta_D}{2} - \sin\frac{\theta_D}{2} + \gamma\frac{\theta_D}{2} \leq 0 \tag{5}$$
$$\alpha = \frac{D}{h_M}\ \text{(Aspect ratio)},\quad \gamma = \frac{h_e}{h_M}\ \text{(Fill ratio)}$$

Figure 2D shows the trend of the maximum $\theta_D$ according to the aspect ratio, $\alpha$ and fill ratio, $\gamma$. The smaller value of $\gamma$ ensures a larger range of $\theta_D$ but it also causes dramatic length variation when the state is changed. It is also possible to achieve a larger range of $\theta_D$ by reducing $\alpha$, but it also reduces the stiffness of the structure which will be discussed in the next section. Additionally, the large $\theta_D$ induces the shear directional tendon force component which may collapse the system. The analysis of the shear forces that the structure can withstand is not addressed in this study because it involves the complex mechanics of granular jamming. However, it is possible to deduce that there is a strong trade-off between the achievable range of $\theta_D$ and the stability of the structure. If the diameter of each disk is small or if the intervals between the disks are large, the structure is likely to become unstable instead of having a higher curvature; if the diameter of the disk is increased or if the interval is shortened, the curvature of the structure is limited but more stable performance can be obtained.

The configuration and reachable space of the continuum structure can be estimated from Equations (3) and (4). We defined the bottom center of the $n$-th unit as the coordinate frame $o_n x_n y_n z_n$ and the top center as $o_{n+1}x_{n+1}y_{n+1}z_{n+1}$ (Fig. 3A). The deformation of the continuum body can be described as the relative movement of these frames, and this transformation can be presented by the rotation direction vector, ${}^n\mathbf{k}$, the rotation angle, ${}^n\theta_D$, and translation vector, ${}^n\mathbf{p}_{n+1}$. We assumed there is no torsion along the backbone of the continuum (Torsion in the $z$-axis is not required for achieving the maximum reachable space), thereby ${}^n\mathbf{k}$ only has $x$- and $y$-axis components. From Rodrigues' rotation formula, the rotation matrix can be presented as:

$$\left[{}^n\mathbf{k}\right]_\times = {}^n\mathbf{K} = \begin{bmatrix} 0 & 0 & {}^nk_y \\ 0 & 0 & -{}^nk_x \\ -{}^nk_y & {}^nk_x & 0 \end{bmatrix}$$
$${}^n\mathbf{R}_{n+1} = \exp({}^n\theta_D\, {}^n\mathbf{K}) \in SO(3) \tag{6}$$

From the condition that ${}^n\mathbf{p}_{n+1}$ should be perpendicular to ${}^n\mathbf{k}$ (no torsion condition), the angle between $z$-axis should be

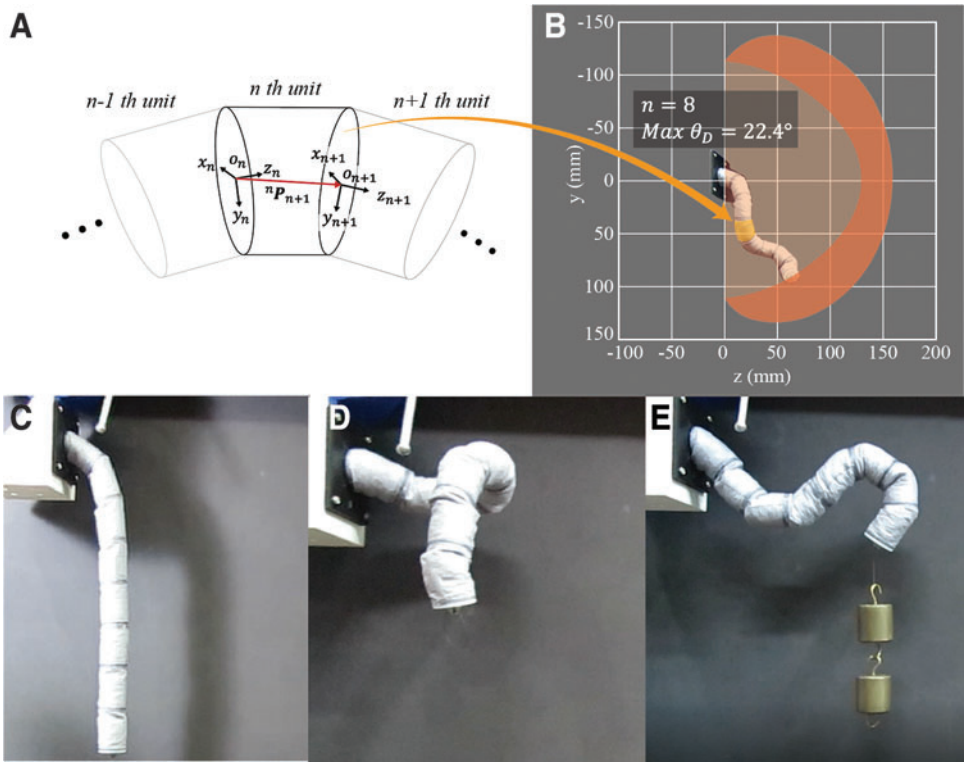


**FIG. 3.** Reachable configuration analysis and implementation. **(A)** Framework and coordinate system design for the configuration estimation. **(B)** Graphical presentation of the reachable space with the condition of $n=8$ and max $\theta_D=22.4°$. **(C)** The structure in the soft state. It cannot support its own weight. **(D)** The stiffened state with helical shape. **(E)** The stiffened state with sinusoidal shape while enduring external forces. Color images are available online.

$\frac{\theta_D}{2}$ [from Eq. (4)], and the length of the vector should be $l$, ${}^n\mathbf{p}_{n+1}$ can be derived as:

$$ {}^n\mathbf{p}_{n+1}\cdot{}^n\mathbf{k}=0,\quad \frac{{}^n\mathbf{p}_{n+1}\cdot{}^n z}{\left|{}^n\mathbf{p}_{n+1}\cdot{}^n z\right|}=\frac{{}^n\theta_D}{2},\quad \left|{}^n\mathbf{p}_{n+1}\right|={}^n l $$

$$ {}^n\mathbf{p}_{n+1}=\begin{pmatrix} -{}^n k_y\ {}^n l\sin\frac{{}^n\theta_D}{2} \\ {}^n k_x\ {}^n l\sin\frac{{}^n\theta_D}{2} \\ {}^n l\cos\frac{{}^n\theta_D}{2}\end{pmatrix} \tag{7} $$

The transformation matrix can be derived from Equations (6) and (7)

$$ ({}^n\mathbf{k},\ {}^n\theta_D)\mapsto {}^nT_{n+1}=\begin{bmatrix} {}^n\mathbf{R}_{n+1} & {}^n\mathbf{p}_{n+1} \\ 0 & 1\end{bmatrix}\in \mathrm{SE}(3) \tag{8} $$

Based on Equation (8), the configuration and reachable space can be estimated with the range of $\theta_D$ and the number of the unit as shown in Figure 3B. The variation on the shape of the continuum body with the standard design parameters (diameter = 25 mm, aspect ratio = 1, and fill ratio = 0.8) is described in Figure 3C–E and Supplementary Video S1.

### Performance Estimation and Evaluation

Although various analysis methods on jamming transitions have been introduced,[25,26,31,52–54] it is difficult to apply these methods to the proposed mechanism because of the complexities of the structures and differences in the working principles. In this study, we present a simplified model for performance estimation. For granular particles to be jammed and behave like solid, compressive stress (positive pressure) needs to be applied to the granular material to induce interlocking between them. The compressive stress maintains entanglement between the particles, which mainly consists of the friction force. Based on this principle, it can be assumed that the tensile stress (negative pressure) applied to the particles would result in a lack of compressive forces between the particles, and the particles will flow like a fluid, which leads to fluidization of the granular particle system.

Figure 4A shows the schematics for estimating the fluidizing point, and Figure 4B presents the experimental setup for simulating fluidization with the force components applied to the structures consisting of compressive stresses induced by the tendon-driven force and distributed stresses induced by the bending force. The bending force (vertical force) at the edge of the unit creates a translational force and torque, but we assumed the fluidized area caused by the torque is a dominant factor in determining the maximum stiffness and ignore the effect of the translational force. To conclude, if the resultant force of the driving force and the external torque acts in the tensile direction, the structure cannot maintain the stiffened state and will not be able to resist an external force.

Based on these assumptions, the maximum stiffness of the mechanism can be estimated from the Euler–Bernoulli beam theory. Pure bending and linear material elasticity conditions were assumed for simplicity without losing the generality of the previous assumptions. The stress distribution induced by the external torque can be expressed as Equation (9), where $\sigma_z$ is the stress induced by the external torque, $M$ is the external torque, and $I$ is the second moment of inertia.

$$ \sigma_z = {}^{Mz}/_{I} \tag{9} $$

If the maximum stress from Equation (9) becomes equal or more than the stress induced by the tendon-driven force, it

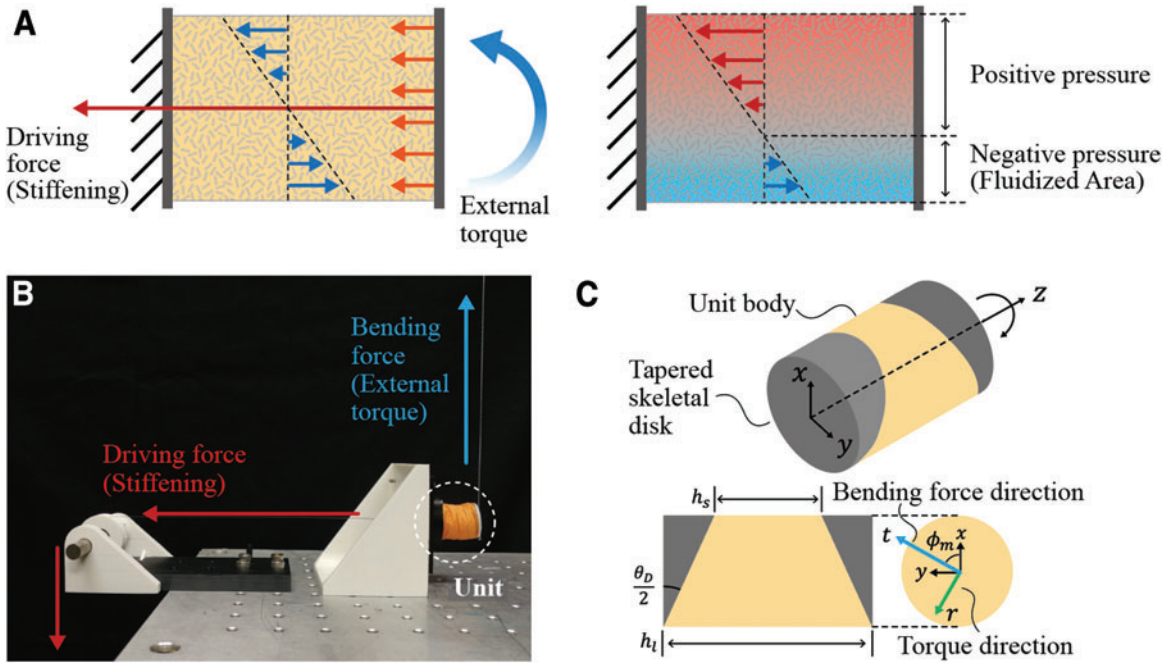


**FIG. 4.** Schematic diagram for the jamming transition estimation and experiment. **(A)** The unit structure under external torque load and tendon driving force, and stress distribution diagram to describe net stress and fluidized area. **(B)** Experimental setup for cantilever beam bending. **(C)** Graphical description of specimen parameters. The specific *in situ* bent angle can be reproduced by changing the taper angle of the skeletal disk. Color images are available online.



will create an area where the particles are fluidized. This reference point can be calculated as shown in Equations (10) and (11), where $\sigma_F$ is the stress induced by the tendon force, $F$ is the driving force exerted by the tendon, $r$ is the radius of the structure, and $A$ is the area of circular cross-section.

$$|\sigma_{z=-r}| = \sigma_F, \quad {}^{rM}/_{I} = \frac{F}{A} \tag{10}$$

Furthermore, when the interlocked area becomes fluidized, it leads to a smaller second moment of inertia and causes a consequent collapse of the structure. In summary, if the presented structure is exposed to external torque, the necessary tendon force to resist it and maintain the intended shape can be estimated using Equation (3).

$$M = \frac{Fr}{4} \tag{11}$$

To evaluate the estimation, a cantilever bending experiment was designed as presented in Figure 4B. From Equation (11), the dominant variables determining the fluidizing points are the diameter of the structure, the driving force. Therefore, in the experiment, the comparison between the estimated value from the model and the actual value of the fluidizing point was made according to the changes in these variables. The experiment was carried out by applying a 10 mm displacement at the end of the specimen in the stiffened state for 60 s in the tangential direction and measuring the force response according to displacement. In addition, to reproduce the condition in various configurations, the specimen model with the bent angle, $\theta_D$ under an external torque was prepared, and the *otr*-coordinate frame was introduced to express the direction of the external torque, which is rotated from the initial frame by $\phi_m$ as shown in Figure 4C.

Assuming that the bending angle induced from the external torque, $\theta$, of the cantilever beam is small, the displacement of the tensile tester, $\delta$, can be expressed as in Equation (12), where $h$ is the height of the specimen. The Euler–Bernoulli beam theory shows the relationship between the external torque, $M$ and the bending angle $\theta$ as the expression presented in Equation (13), where $E$ is the elastic modulus, and $I$ is the area moment of inertia.

$$\delta \approx {}^{h\,\theta}/_{2} \tag{12}$$

$$M_{ext} = {}^{EI\,\theta}/_{h} \tag{13}$$

From Equations (12) and (13), the relationship between the bending stiffness, external torque, and displacement can be derived as in Equation (14), where $T$ is the pulling force of the tensile tester. Equation (14) implies that the differential value of the applied force to displacement is proportional to the bending stiffness. Since the bending stiffness of the structure decreases after fluidization, the maximum point of the differential value of the data can be regarded as the actual fluidization point.

$$Th = M = \frac{2EI}{h^2}\delta, \quad \max EI = \max \frac{h^3}{2}\frac{dT}{d\delta} \tag{14}$$

A tensile tester (UNITECH, RB302 Microload) and load cell (DACELL, UMM-K100) were used for the experiments. Nine specimens with zero $\theta_D$ were prepared to

evaluate the effect of the diameter. The values of the diameter of these specimens were 20, 25, and 30 mm. For each diameter, specimens with heights of 20, 25, and 30 mm were made. But the heights were recorded for each experiment sequence to avoid the differences caused by the placement variations of granular particles. The driving force was applied by attaching the weight vertically using a pulley at the end of the tendon. The driving weight was applied from 2 to 6.5 kgf at intervals of 1.5 kgf. To evaluate the effect of $\theta_D$ and $\phi_m$, the specimens with 25 mm diameter and height were made with 10° and 20° of $\theta_D$, each was tested with $\phi_m$ of 0°, 90°, and 180°. The experiments were repeated 3 times for each condition, and in total, 180 experiments were conducted.

Figure 5A shows the result of the force and displacement of the specimen of zero $\theta_D$, 25 mm diameter, and height after stiffening with 2 kgf of the driving force. The black line shows the force exerted by the tensile tester, and the red line shows the differential value of the applied force that represents the bending stiffness from Equation (14). From the maximum value of the red line, the value of the external torque where fluidization occurs can be acquired. Figure 5B shows the effect of the diameter of the specimen on the fluidizing point. The box plot represents the value of the external torque at the fluidizing point, which is normalized by the driving force, and the red line represents the estimated value at fluidizing from Equation (11). Figure 5C shows the effect of the driving force on the fluidizing point. In this study, the value of the external torque is normalized by the diameter and compared with the result estimated from Equation (11). The results of the proposed estimation show a tendency similar to the actual behavior of the structure. The limits of the external torque required to maintain shape are linearly related to the driving force, and the ratio of this relation is determined by the geometric conditions of the structure. By increasing the diameter, the unit structure can endure higher external torque.

Figure 5D shows the effect of $\theta_D$ and $\phi_m$ of the specimen with 25 mm diameter and height on the fluidizing point. Asymmetrical geometry is expected to exacerbate stress concentrations, causing structures to collapse earlier, but it is difficult to theoretically predict this phenomenon. Nevertheless, these data can suggest design guidelines by reproducing the worst conditions that show the most dramatic torque limit reduction. Regardless of the torque direction, the torque limit decreases significantly with the bent angle, and it shows a 34% reduction in the worst case. As a higher bent angle requires a higher driving force to endure external torque, a designer can change the height and fill ratio of unit structure to adjust the maximum bent angle. Therefore, the design parameters (diameter, height, and fill ratio) can be determined in advance according to the expected use condition, including the intended working range and the capacity of the driving force.

## Discussion

In this work, we propose an electric motor-tendon-based granular jamming mechanism for variable stiffness. To overcome the differences between tendon- and vacuum-driven systems, the design conditions have been derived and solutions have been provided. The stiffening characteristics and geometrical considerations were also addressed in these contexts. In addition to these considerations, the design guidelines through theoretical analysis and

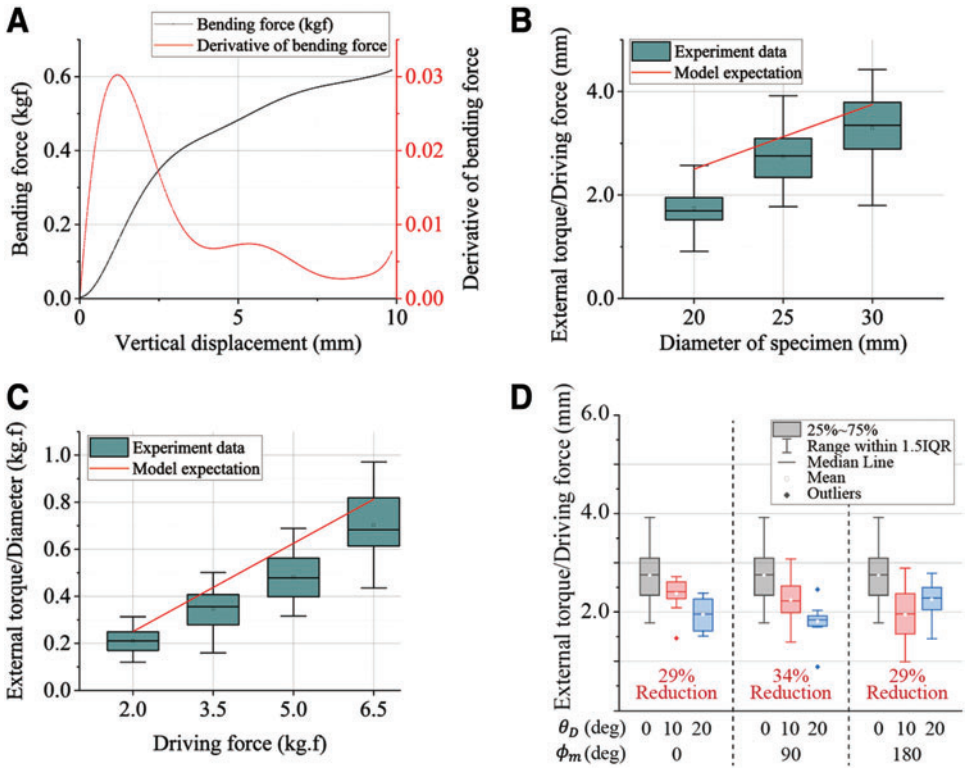


**FIG. 5.** Performance evaluation results. **(A)** Results of the specimen with 25 mm diameter and height, which was stiffened by 2 kgf driving force. **(B)** Estimated value from analysis (*red*) and experimented value (*box plot*) about diameter-external torque/driving force and **(C)** driving force-external torque/diameter. **(D)** Effect of bent angle and torque direction on torque limit acquired from the specimen with the tapered skeletal disk. The numbers in *red* indicate the reduction in the lowest mean value relative to the highest. Color images are available online.

supporting experiments were proposed for performance evaluation.

The proposed mechanism in this article is encouraging in that it can achieve high stiffness changes with smaller structures and actuators with different form factors as compared with common vacuum jamming. We believe that these features have a high potential for the variable stiffness mechanism for soft wearable robots. To demonstrate this possibility, a wrist-type variable stiffness wearable device was fabricated using the proposed structure (Fig. 6 and Supplementary Video S2). Three of the 150-mm-long variable stiffness mechanisms were placed at regular intervals on an 85 mm diameter circle and could change the stiffness according to the electrical signal to protect the wrist by performing the strutting function of the muscles instead. The weight of each variable stiffness mechanism is 54 g, including the actuator, and the weight of the whole structure is 184 g, including the base wrist support. Furthermore, it can change its own stiffness within 2 s and uses 10 W power to support 2 kgf.

While the proposed mechanism could have high potential, there is still room for improving the performance. Since the scope of this study is to propose a novel mechanism and to demonstrate its possibilities, there were assumptions or issues that were not considered in depth. If a more accurate relationship between the compressive stress and elastic modulus of the structure can be derived, the estimation of the stiffness properties of this structure will be more accurate, which will enable better performance in design optimization. The selection of more suitable granular materials for the electric motor-tendon drive and investigation of the effect of more geometric parameters will also be important issues for performance improvement. In addition, we currently use only one tendon for each variable stiffness structure but using a combination of multiple tendons in various directions may enable widening the configurable range of the proposed concept.

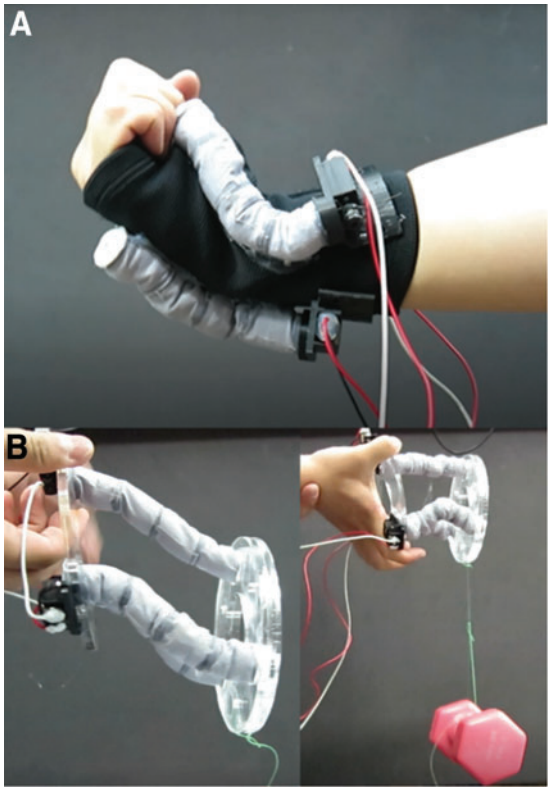


**FIG. 6.** A wrist-type variable stiffness wearable device. **(A)** Wearable device worn on the wrist. Various wrist motions are possible without a large resistance. **(B)** Stiffness difference validation model of proposed wrist-assistive device (*left*: low stiffness, *right*: high stiffness). In the stiffened state, the structure is capable of withstanding a weight of 2 kgf or more. Color images are available online.

### Author Disclosure Statement

No competing financial interests exist.

### Funding Information

This material is based upon work supported by the National Research Foundation of Korea (NRF) Grant funded by the Korean Government (MSIP) (No. NRF-2016R1A5A1938472), the KIST Institutional Program (No. 2V07080-19-P073), and 2019 Research Grant from Kangwon National University.

### Supplementary Material

Supplementary Video S1
Supplementary Video S2

### References

1. Shepherd RF, Ilievski F, Choi W, *et al.* Multigait soft robot. Proc Natl Acad Sci USA 2011;108:20400–20403.
2. In H, Kang BB, Sin M, *et al.* Exo-Glove: A wearable robot for the hand with a soft tendon routing system. IEEE Robot Automat Mag 2015;22:97–105.
3. Laschi C, Mazzolai B, Cianchetti M. Soft robotics: Technologies and systems pushing the boundaries of robot abilities. Sci Robot 2016;1:eaah3690.
4. Manti M, Cacucciolo V, Cianchetti M. Stiffening in soft robotics: A review of the state of the art. IEEE Robot Automat Mag 2016;23:93–106.
5. Wang L, Yang Y, Chen Y, *et al.* Controllable and reversible tuning of material rigidity for robot applications. Mater Today 2018;21:563–576.
6. Rich S, Jang SH, Park YL, *et al.* Liquid metal-conductive thermoplastic elastomer integration for low-voltage stiffness tuning. Adv Mater Technol 2017;2:1700179.
7. Firouzeh A, Salerno M, Paik J. Stiffness control with shape memory polymer in underactuated robotic origamis. IEEE Trans Robot 2017;33:765–777.
8. Yang Y, Chen Y, Li Y, *et al.* Novel variable-stiffness robotic fingers with built-in position feedback. Soft Robot 2017;4:338–352.
9. Cheng NG, Gopinath A, Wang L, *et al.* Thermally Tunable, Self-Healing Composites for Soft Robotic Applications. Macromol Mater Eng 2014;229:1279–1284.
10. Schubert BE, Floreano D. Variable stiffness material based on rigid low-melting-point-alloy microstructures embedded in soft poly(dimethylsiloxane) (PDMS). RSC Adv 2013;3:24671–24679.

11. Shintake J, Schubert B, Rosset S, *et al.* Variable stiffness actuator for soft robotics using dielectric elastomer and low-melting-point alloy. In: IEEE/RSJ International Conference on Intelligent Robots and Systems (IROS), Hamburg, Germany. Piscataway, NJ: IEEE, 2015:1097–1102.
12. Tonazzini A, Mintchev S, Schubert B, *et al.* Variable stiffness fiber with self-healing capability. Adv Mater 2016; 28:10142–10148.
13. Kim JS, Lee DY, Koh JS, *et al.* Component assembly with shape memory polymer fastener for microrobots. Smart Mater Struct 2013;23:015011
14. Kim SJ, Lee DY, Jung GP, *et al.* An origami-inspired, self-locking robotic arm that can be folded flat. Sci Robot 2018; 3:eaar2915.
15. Oliveira MB, Liu C, Zhao M, *et al.* Design of a variable stiffness wrist brace with an origami structural element. In: ASME Conference on Smart Materials, Adaptive Structures and Intelligent Systems, San Antonio, Texas, USA. New York, NY: ASME, 2018:V002T08A009.
16. Park YJ, Lee JG, Jeon S, *et al.* Dual-stiffness structures with reconfiguring mechanism: Design and investigation. J Intell Mater Syst Struct 2016;27:995–1010
17. Mintchev S, Shintake J, Floreano D. Bioinspired dual-stiffness origami. Sci Robot 2018;3:eaau0275.
18. Behbahani SB, Tan X. Design and dynamic modeling of electrorheological fluid-based variable-stiffness fin for robotic fish. Smart Mater Struct 2017;26:085014.
19. Majidi C, Wood RJ. Tunable elastic stiffness with microconfined magnetorheological domains at low magnetic field. Appl Phys Lett 2010;97:164104.
20. Wakimoto S, Kumagai I, Suzumori K. Development of large intestine endoscope changing its stiffness. In: IEEE International Conference on Robotics and Biomimetics (ROBIO), Guilin, China. Piscataway, NJ: IEEE, 2009: 2320–2325.
21. Suzumori K, Wakimoto S, Miyoshi K, *et al.* Long bending rubber mechanism combined contracting and extending fluidic actuators. In: IEEE/RSJ International Conference on Intelligent Robots and Systems, Tokyo, Japan. Piscataway, NJ: IEEE, 2013:4454–4459.
22. Shiva A, Stilli A, Noh Y, *et al.* Tendon-based stiffening for a pneumatically actuated soft manipulator. IEEE Robot Automat Lett 2016;1:632–637.
23. Huh TM, Park YJ, Cho KJ. Design and analysis of a stiffness adjustable structure using an endoskeleton. Int J Precis Eng Manuf 2012;13:1255–1258.
24. Park YJ, Huh TM, Park D, *et al.* Design of a variable-stiffness flapping mechanism for maximizing the thrust of a bio-inspired underwater robot. Bioinspir Biomim 2014;9: 036002.
25. Liu AJ, Nagel SR. Nonlinear dynamics: Jamming is not just cool any more. Nature 1998;396:21–22.
26. Majmudar TS, Sperl M, Luding S, *et al.* Jamming transition in granular systems. Phys Rev Lett 2007;98:058001.
27. Trappe V, Prasad V, Cipelletti L, *et al.* Jamming phase diagram for attractive particles. Nature 2001;411: 772–775.
28. Brown E, Rodenberg N, Amend J, *et al.* Universal robotic gripper based on the jamming of granular material. Proc Natl Acad Sci USA 2010;107:18809–18814.
29. Wei Y, Chen Y, Ren T, *et al.* A Novel, Variable stiffness robotic gripper based on integrated soft actuating and particle jamming. Soft Robot 2016;3:134–143.
30. Amend J, Lipson H. The JamHand: Dexterous manipulation with minimal actuation. Soft Robot 2017;4:70–80.
31. Steltz E, Mozeika A, Rodenberg N, *et al.* JSEL: Jamming Skin Enabled Locomotion. In: IEEE/RSJ International Conference on Intelligent Robots and Systems, St. Louis, MO, USA. Piscataway, NJ: IEEE, 2009:5672–5677.
32. Wall V, Deimel R, Brock O. Selective stiffening of soft actuators based on jamming. In: IEEE International Conference on Robotics and Automation, Seattle, WA, USA. Piscataway, NJ: IEEE, 2015:252–257.
33. Thompson-Bean E, Steiner O, McDaid A. A soft robotic exoskeleton utilizing granular jamming. In: IEEE International Conference on Advanced Intelligent Mechatronics, Busan, South Korea. Piscataway, NJ: IEEE, 2015:165–170.
34. Cheng NG, Lobovsky MB, Keating SJ, *et al.* Design and Analysis of a Robust, Low-cost, Highly Articulated manipulator enabled by jamming of granular media. In: IEEE International Conference on Robotics and Automation, St. Paul, MN, USA. Piscataway, NJ: IEEE, 2012:4328–4333.
35. Falco ID, Cianchetti M, Menciassi A. A soft multi-module manipulator with variable stiffness for minimally invasive surgery. Bioinspir Biomim 2017;12:056008.
36. Hauser S, Robertson M, Ijspeert A, *et al.* JammJoint: A variable stiffness device based on granular jamming for wearable joint support. IEEE Robot Automat Lett 2017;2: 849–855.
37. Jiang A, Ataollahi A, Althoefer K, *et al.* A variable stiffness joint by granular jamming. In: ASME. International Design Engineering Technical Conferences and Computers and Information in Engineering Conference, Chicago, Illinois, USA, vol. 4. New York, NY: ASME, 2012:267–275.
38. Li M, Ranzani T, Sareh S, *et al.* Multi-fingered haptic palpation utilizing granular jamming stiffness feedback actuators. Smart Mater Struct 2014;23:095007.
39. Hauser S, Mutlu M, Banzet P, *et al.* Compliant universal grippers as adaptive feet in legged robots. Adv Robot 2018; 32:825–836.
40. Hauser S, Mutlu M, Freundler F, *et al.* Stiffness variability in jamming of compliant granules and a case study application in climbing vertical shafts. In: IEEE International Conference on Robotics and Automation, Brisbane, QLD, Australia. Piscataway, NJ: IEEE, 2018:1559–1566.
41. Stanley AA, Gwilliam JC, Okamura AM, Haptic jamming: A deformable geometry, variable stiffness tactile display using pneumatics and particle jamming. In: World Haptics Conference, Daejeon, South Korea. Piscataway, NJ: IEEE, 2013:25–30.
42. Bajkowski JM, Dyniewicz B, Bajer CI. Damping properties of a beam with vacuum-packed granular damper. J Sound Vib 2015;341:74–85.
43. Miller-Jackson T, Sun Y, Natividad R, *et al.* Tubular Jamming: A variable stiffening method toward high-force applications with soft robotic components. Soft Robot 2019;6:468–482.
44. Jiang Y, Chen D, Liu C, *et al.* Chain-like granular jamming: A novel stiffness-programmable mechanism for soft robotics. Soft Robot 2019;6:118–132.
45. Kim YJ, Cheng S, Kim S, *et al.* A novel layer jamming mechanism with tunable stiffness capability for minimally invasive surgery. Trans Robot 2013;29:1031–1042.
46. Ou J, Yao L, Tauber D, *et al.* jamSheets: Thin interfaces with tunable stiffness enabled by layer jamming. In Proceedings of the 8th International Conference on Tangible,

Embedded and Embodied Interaction, Munich, Germany. New York, NY: Association for Computing Machinery, 2014;65–72.
47. Narang YS, Vlassak JJ, Howe RD. Mechanically versatile soft machines through laminar jamming. Adv Funct Mater 2018;28:1707136.
48. Santiago JLC, Godage IS, Gonthina P, *et al.* Soft robots and kangaroo tails: Modulating compliance in continuum structures through mechanical layer jamming. Soft Robot 2016;3:54–63.
49. Choi WH, Kim S, Lee D, *et al.* Soft, multi-DoF, variable stiffness mechanism using layer jamming for wearable robots. IEEE Robot Autom Lett 2019;4:2539–2546.
50. Choi I, Corson N, Peiros L, *et al.* A soft, controllable, high force density linear brake utilizing layer jamming. IEEE Robot Autom Lett 2017;3:450–457.
51. Jiang A, Aste T, Dasgupta P, *et al.* Granular jamming transitions for a robotic mechanism. AIP Conference Proceedings 2013;1542:385–388.
52. Jaeger HM, Nagel SR, Behringer RP. Granular solids, liquids, and gases. Rev Modern Phys 1996;68:1259.
53. Cates M, Wittmer J, Bouchaud JP, *et al.* Jamming, force chains, and fragile matter. Phys Rev Lett 1998;81:1841.
54. Hecke MV. Jamming of soft particles: Geometry, mechanics, scaling and isostaticity. J Phys Condens Matter 2009;22:033101.

Address correspondence to:
*Yong-Jai Park*
*Department of Mechatronics*
*Kangwon National University*
*1, Gangwondaehak-gil*
*Chuncheon-si*
*Gangwon-do 24341*
*Korea*

*E-mail:* yjpark@kangwon.ac.kr

*Kyu-Jin Cho*
*Department of Mechanical and Aerospace Engineering*
*Seoul National University*
*1, Gwanak-ro*
*Gwanak-gu*
*Seoul 08826*
*Korea*

*E-mail:* kjcho@snu.ac.kr